THE JOURNAL OF PHYSICAL CHEMISTRY Letters

pubs.acs.org/JPCL Letter

Plane-Selective Coating of Li_2SnO_3 on $Li[Ni_xCo_{1-x}]O_2$ for High Power Li ion Batteries

Hanseul Kim,[#] Garam Choi,[#] Seongmin Kim,[#] Donghoon Lee, Sung Wook Doo, Jungwon Park, Won Bo Lee,* and Kyu Tae Lee*

Cite This: *J. Phys. Chem. Lett.* 2020, 11, 7096−7102 Read Online

ACCESS | Metrics & More | Article Recommendations | Supporting Information

ABSTRACT: Interphase engineering is becoming increasingly important in improving the electrochemical performance of cathode materials for rechargeable batteries, including Li ion, Li metal, and all-solid-state batteries, because irreversible surface reactions, such as electrolyte decomposition, and transition metal dissolution, constitute one of these batteries' failure modes. In this connection, various surface-engineered cathode materials have been investigated to improve interfacial properties. No synthesis methods, however, have considered a plane-selective surface modification of cathode materials. Herein, we introduce the basal-plane-selective coating of Li_2SnO_3 on layered $Li[Ni_xCo_{1-x}]O_2$ (x = 0 and 0.5) using the concept of the thermal phase segregation of Sn-doped $Li[Ni_xCo_{1-x}]O_2$ due to the solubility variation of Sn in $Li[Ni_xCo_{1-x}]O_2$ with respect to temperature. The plane-selective surface modification enables the formation of Li_2SnO_3 nanolayers on only the $Li[Ni_xCo_{1-x}]O_2$ basal plane without hindering the charge transfer of Li^+ ions. As a result, the vertical heterostructure of $Li[Ni_xCo_{1-x}]O_2$−Li_2SnO_3 core−shells show promising electrochemical performance.

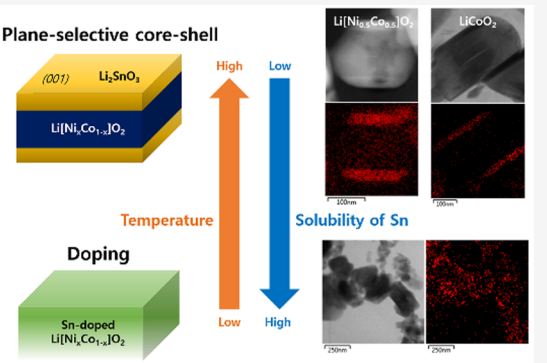

Interphase engineering is becoming increasingly important in improving the electrochemical performance of rechargeable batteries, such as Li ion, Li metal, and all-solid-state batteries, because irreversible surface reactions are now known to play a crucial role in these batteries' failures.[1−15] For example, substantial electrolyte decomposition and transition metal dissolution occur on the cathode surface at high voltages and temperatures, resulting in a severe fading of capacity.[16−19] Therefore, various surface-engineered cathode materials have been investigated to suppress these irreversible surface reactions.[20−23] In this connection, a variety of surface modification techniques have been developed for cathode materials, including sol−gel synthesis, dry coating, and atomic layer deposition.[24−28] However, most methods were not able to modify the cathode surface plane-selectively.[29,30] Herein, we introduced the basal-plane-selective coating of Li_2SnO_3 on $Li[Ni_xCo_{1-x}]O_2$ using the thermal phase segregation of Sn-doped $Li[Ni_xCo_{1-x}]O_2$ due to the solubility variation of Sn in Sn-doped $Li[Ni_xCo_{1-x}]O_2$ with respect to temperature. Sn was easily doped in $Li[Ni_xCo_{1-x}]O_2$ at ca. 700 °C, leading to the formation of $Li[Sn_zNi_xCo_{1-x-z}]O_2$. However, Sn-doped $Li[Ni_xCo_{1-x}]O_2$ decomposed to a mixture of Li_2SnO_3 and $Li[Ni_xCo_{1-x}]O_2$ at temperatures higher than ca. 700 °C because of the poor solubility of Sn in $Li[Ni_xCo_{1-x}]O_2$ at higher temperatures. This is attributed to the fact that the mixture of xLi_2SnO_3 and $(1 - x)Li[Ni_xCo_{1-x}]O_2$ is thermodynamically more stable than $Li[Sn_zNi_xCo_{1-x-z}]O_2$ at these higher temperatures. During the phase segregation at high temperatures, Li_2SnO_3 nanolayers were grown basal-plane-selectively on the $Li[Sn_zNi_xCo_{1-x-z}]O_2(001)$ surface, forming the vertical heterostructure of basal-plane-selective $Li[Ni_xCo_{1-x}]O_2$−Li_2SnO_3 core−shells. To demonstrate the basal-plane-selective coating of Li_2SnO_3 on $Li[Ni_xCo_{1-x}]O_2$, we performed various atomic-scale analyses such as scanning transmission electron microscopy (STEM) with a high-angle annual dark field (HAADF) mode, fast Fourier transformation (FFT), and energy dispersive X-ray spectroscopy (EDS). We also carried out the density functional theory (DFT) calculation to clarify the origin of the phase segregation of $Li[Sn_xCo_{1-x}]O_2$ at temperatures higher than 700 °C. Moreover, we compared the electrochemical performance of plane-selective $LiCoO_2$−Li_2SnO_3 core−shells with that of conventional sol−gel-derived Li_2SnO_3-coated $LiCoO_2$ to demonstrate the role of the plane-selective surface modification in the electrochemical performance of $LiCoO_2$ at high charge cutoff voltages.

Scheme 1 shows the schematic concept of the basal-plane-selective coating of Li_2SnO_3 on $Li[Ni_xCo_{1-x}]O_2$ due to the

Received: June 12, 2020
Accepted: August 4, 2020
Published: August 4, 2020

https://dx.doi.org/10.1021/acs.jpclett.0c01829
J. Phys. Chem. Lett. 2020, 11, 7096−7102

Scheme 1. Schematic Concept for the Synthesis of Plane-Selective $Li[Ni_xCo_{1-x}]O_2$–Li_2SnO_3 Core-Shells

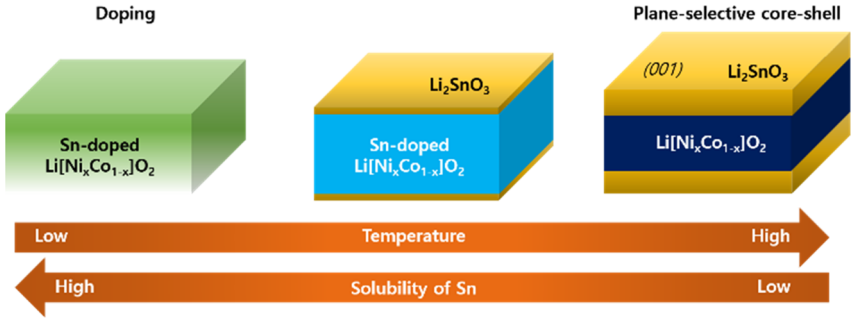

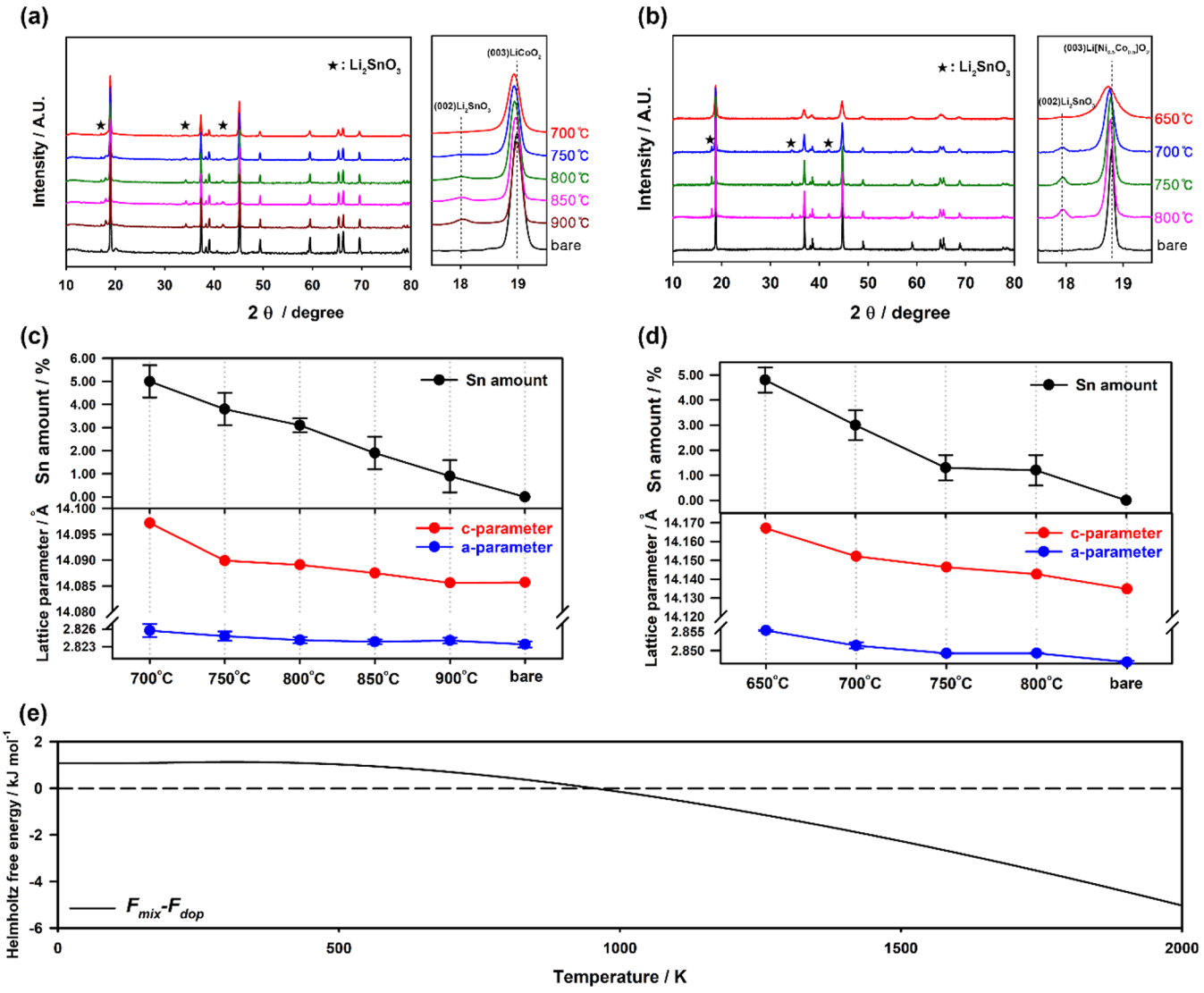

Figure 1. XRD patterns of bare $LiCoO_2$ and 5 at. % Sn-added $Li[Ni_xCo_{1-x}]O_2$ at various heating temperatures: (a) $x = 0$ and (b) $x = 0.5$. (c), (d) Rietveld refinement results of XRD patterns in (a) and (b), respectively. (e) Theoretical Helmholtz free energy difference between $zLi_2SnO_3 + (1 - z)LiCoO_2$ (F_{mix}) and $Li[Sn_zCo_{1-z}]O_2$ (F_{dop}).

solubility variation of Sn in $Li[Ni_xCo_{1-x}]O_2$ with respect to temperature. When the sol–gel precursors of $LiNO_3$, Ni-$(NO_3)_2{\cdot}6H_2O$, Co$(NO_3)_2{\cdot}6H_2O$, $SnCl_2$, and citric acid were heated at 650–700 °C, 5 at. % Sn-doped $Li[Ni_xCo_{1-x}]O_2$ ($x = 0$ and 0.5, space group: $R\bar{3}m$) was obtained without impurities, as shown in its X-ray diffraction (XRD) pattern (Figure 1a,b). However, β-Li_2SnO_3 (space group: $C12/c1$) appeared above 700 °C, and its XRD peak intensities increased gradually as the heating temperature increased from 700 °C (Figure 1a,b). This indicates that Sn-doped $Li[Ni_xCo_{1-x}]O_2$ gradually decomposed to β-Li_2SnO_3 and $Li[Ni_xCo_{1-x}]O_2$ with increasing temperature above 700 °C. This is further supported by changes in the (003) plane peak positions of Sn-doped $Li[Ni_xCo_{1-x}]O_2$ ($x = 0$ and 0.5) with increasing temperature.

https://dx.doi.org/10.1021/acs.jpclett.0c01829
J. Phys. Chem. Lett. 2020, 11, 7096–7102

The (003) plane peak position of Sn-doped $LiCoO_2$ obtained at 700 °C is lower in 2θ than that of bare $Li[Ni_xCo_{1-x}]O_2$. This is attributed to the fact that the (003) plane of Sn-doped $Li[Ni_xCo_{1-x}]O_2$ expanded because of the replacement of Co^{3+} (radius: 0.545 Å) and Ni^{3+} ions (radius: 0.56 Å) with larger Sn^{4+} ions (radius: 0.69 Å) in $Li[Ni_xCo_{1-x}]O_2$. However, the (003) plane peak positions of Sn-doped $Li[Ni_xCo_{1-x}]O_2$ gradually shifted to the higher 2θ with increasing temperature, and eventually, the XRD peak positions of the samples obtained at 900 and 800 °C were almost the same as those of bare $Li[Ni_xCo_{1-x}]O_2$ (x = 0 and 0.5, respectively).

We performed Rietveld refinement to estimate the amount of Sn in Sn-doped $Li[Ni_xCo_{1-x}]O_2$ and the lattice parameters, as shown in Figure 1c,d. The amount of z in $Li[Sn_z(Ni_xCo_{1-x})_{1-z}]O_2$ (x = 0) decreased from 4.9 ± 0.7% to 0.8 ± 0.7% with increasing temperature from 700 to 900 °C. The amount of z in $Li[Sn_z(Ni_xCo_{1-x})_{1-z}]O_2$ (x = 0.5) also decreased from 4.8 ± 0.5% to 1.2 ± 0.6% with increasing temperature from 650 to 800 °C. As a result, the lattice parameter c of $Li[Sn_zCo_{1-z}]O_2$ decreased with increasing temperature. The lattice parameter c values of $Li[Sn_z(Ni_xCo_{1-x})_{1-z}]O_2$ (x = 0 and 0.5) obtained at 900 and 800 °C, respectively, were almost the same as that of bare $LiCoO_2$. This reveals that the solubility of Sn in $Li[Sn_z(Ni_xCo_{1-x})_{1-z}]O_2$ decreases with increasing temperature, eventually leading to the phase segregation of $Li[Sn_z(Ni_xCo_{1-x})_{1-z}]O_2$ into two phases of of Li_2SnO_3 and $Li[Ni_xCo_{1-x}]O_2$ at high temperatures.

We performed DFT calculations to demonstrate the thermal phase segregation of $Li[Sn_zCo_{1-z}]O_2$. Figure 1e shows the difference between the Helmholtz free energies ($F_{mix} - F_{dop}$) of $zLi_2SnO_3 + (1 - z)LiCoO_2$ (F_{mix}) and $Li[Sn_zCo_{1-z}]O_2$ (F_{dop}); z is assumed to be 0.08 in the calculation, which corresponds to a substitution of one of Co atoms by Sn in the 2 × 2 supercell of $LiCoO_2$. The crystal structures and Helmholtz free energies of Li_2SnO_3, $LiCoO_2$, and $Li[Sn_{0.08}Co_{0.92}]O_2$ are displayed in Figure S1. The value of $F_{mix} - F_{dop}$ is positive at temperatures below ca. 1000 K, implying that Sn-doped $LiCoO_2$ is thermodynamically more stable than the mixture of zLi_2SnO_3 and $(1 - z)LiCoO_2$ at these temperatures. This is consistent with our experimental results, where Sn-doped $LiCoO_2$ was obtained without impurities at 700 °C (973.15 K). The value of $F_{mix} - F_{dop}$, however, decreases with increasing temperature. Eventually, this value turns from positive to negative at ca. 1000 K. This indicates that the mixture of zLi_2SnO_3 and $(1 - z)LiCoO_2$ is thermodynamically more stable than Sn-doped $LiCoO_2$ at greater than ca. 1000 K. This supports the results that the mixture of Li_2SnO_3 and $LiCoO_2$ was obtained at temperatures above 700 °C.

We compared the cross-sectional STEM and the corresponding EDS mapping images of plane-selective $Li[Ni_xCo_{1-x}]O_2$–Li_2SnO_3 core–shells (Figure 2). Cross-sectional thin STEM specimens were obtained using an Ar ion slicer. Sn-doped $Li[Ni_xCo_{1-x}]O_2$ particles are several hundreds of nanometers in size, with plate-like morphology in the form of a single crystal, as shown in their SEM images (Figure S2). The (001) plane surface energy of $LiCoO_2$ is known to be lower than the surface energies of other planes (i.e., (104) and (012)) in oxidizing atmospheres, resulting in the formation of plate-like powders.[31] When Sn-doped $Li[Ni_xCo_{1-x}]O_2$ (x = 0) was heated at 700 °C, Sn was uniformly distributed and overlapped with Co in a particle, as shown in Figure 2a. This indicates that Sn was doped in $LiCoO_2$. At 900 °C, however,

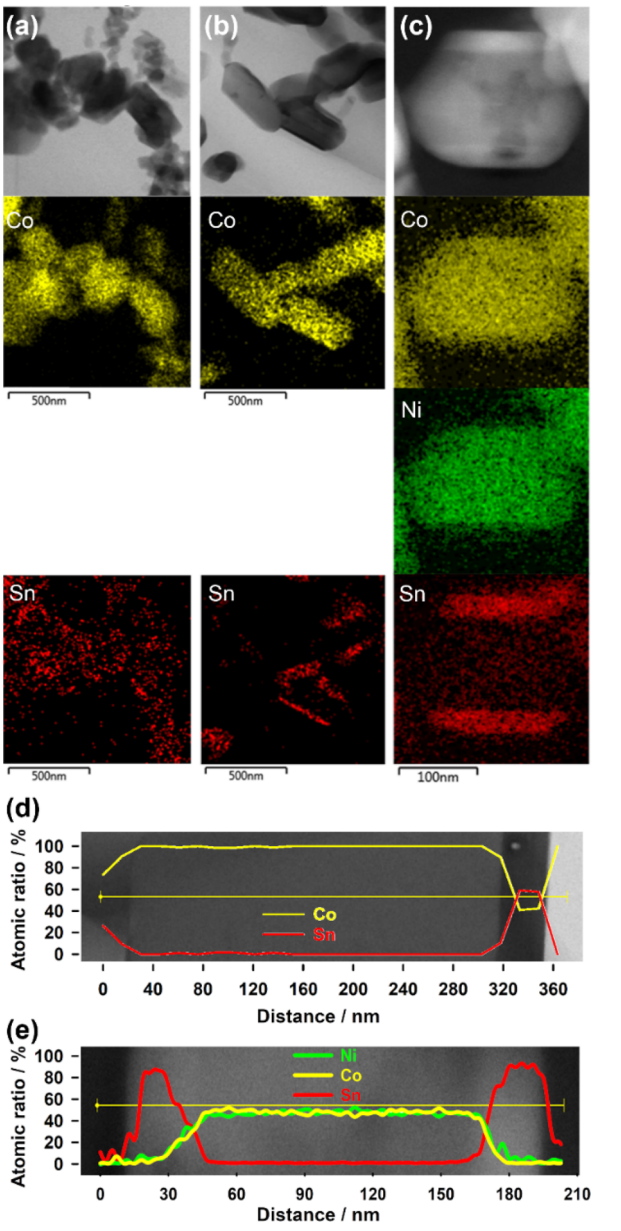

Figure 2. Cross-sectional STEM and corresponding EDS mapping images of (a) 5 at. % Sn-doped $Li[Ni_xCo_{1-x}]O_2$ (x = 0) heated at 700 °C, (b) plane-selective $Li[Ni_xCo_{1-x}]O_2$–Li_2SnO_3 (x = 0) heated at 900 °C, and (c) plane-selective $Li[Ni_xCo_{1-x}]O_2$–Li_2SnO_3 (x = 0.5) heated at 800 °C. Cross-sectional STEM-EDS line profiles of plane-selective $Li[Ni_xCo_{1-x}]O_2$–Li_2SnO_3 core–shells for (d) x = 0 and (e) x = 0.5.

Sn and Co are clearly separated, where Co is located in the inside region and Sn in the outside region of a particle (Figure 2b). Considering their XRD patterns (Figure 1a), this suggests that Li_2SnO_3 nanolayers were segregated outside $LiCoO_2$ at 900 °C. Moreover, it is remarkable that Li_2SnO_3 did not cover all facets of a $LiCoO_2$ particle. Li_2SnO_3 layers were selectively and uniformly grown only on the specific plane of $LiCoO_2$. This selective segregation behavior was generally observed in all particles (see more STEM images in Figure S3). The same plane-selective phase segregation was also observed in 5 at. % Sn-added $Li[Ni_xCo_{1-x}]O_2$ (x = 0.5) heated at 800 °C (Figure 2c). The thickness of Li_2SnO_3 layers in $Li[Ni_xCo_{1-x}]O_2$–

https://dx.doi.org/10.1021/acs.jpclett.0c01829
J. Phys. Chem. Lett. 2020, 11, 7096–7102

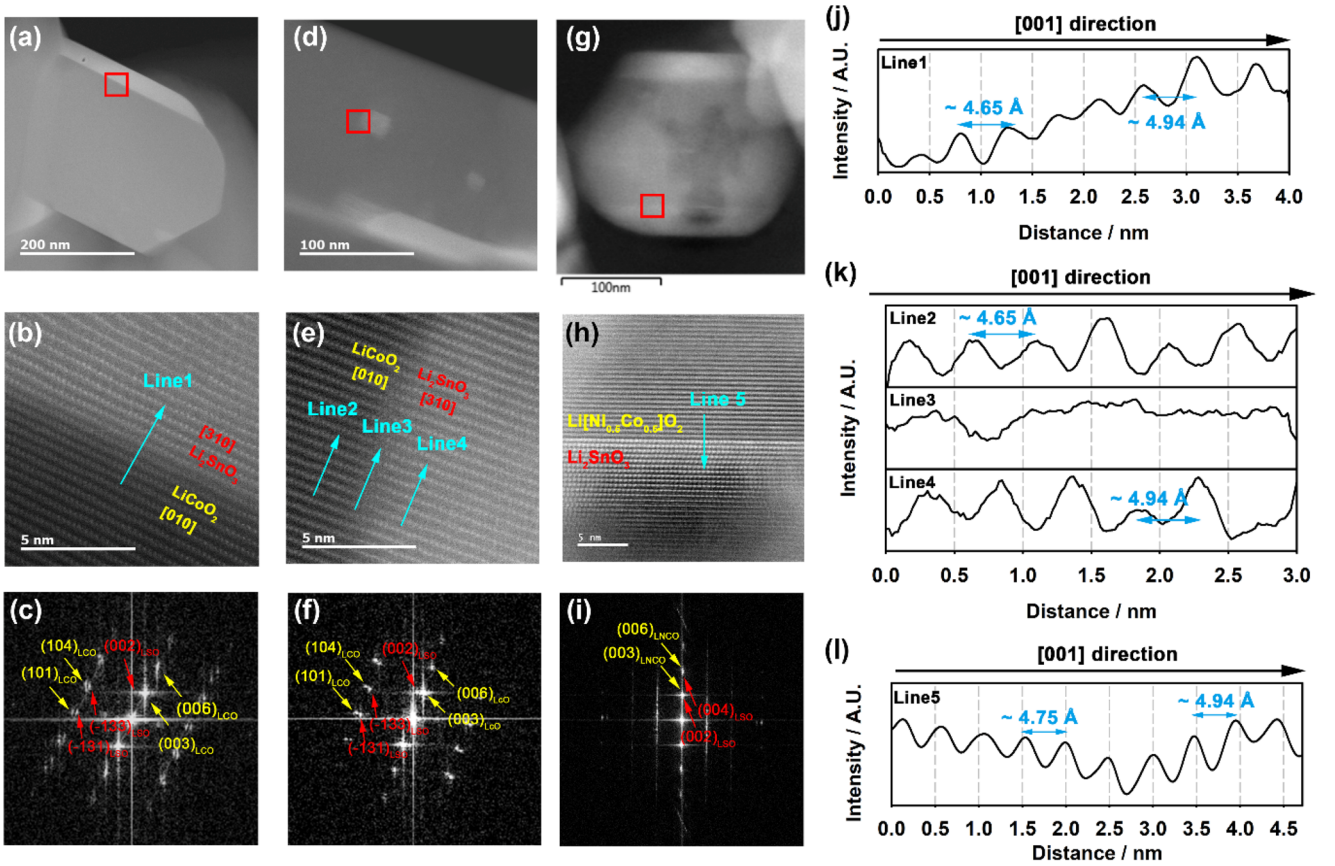

Figure 3. STEM analysis of $Li[Ni_xCo_{1-x}]O_2$–Li_2SnO_3 core–shells with different cooling rates and composition: (a)–(c) $x = 0$ with 1 °C min^{-1} (d)–(f) $x = 0$ with quenching and (g)–(i) $x = 0.5$ with 1 °C min^{-1}. (a), (d), (g) Z-contrast HAADF images. (b), (e), (h) Enlarged Z-contrast HAADF images of red squares in (a, d, g), respectively. (c), (f), (i) FFT patterns of (b, e, h) images, respectively. (j) Line profile of the STEM image intensity across the interface through line 1 along the [001] direction in (b). (k) Line profiles of the STEM image intensity through line 2, 3, and 4 in (e). (l) Line profile of the STEM image intensity across the interface through line 5 along the [001] direction in (h).

Li_2SnO_3 core–shells was approximately 20–30 nm, as shown in their EDS line profiles (Figure 2d,e).

To investigate the plane-selective segregation mechanism of Li_2SnO_3 on $Li[Ni_xCo_{1-x}]O_2$, we compared the cross-sectional high-angle annular dark field (HAADF)-STEM images of 5 at. % Sn-added $Li[Ni_xCo_{1-x}]O_2$ ($x = 0$) obtained at different cooling rates (Figure 3). Panels a and d of Figure 3, respectively, show the Z-contrast HAADF-STEM images of the slowly cooled (1 °C/min) samples and those of the quenched samples. The bright gray and the dark gray regions correspond to Li_2SnO_3 and $LiCoO_2$, respectively, because the atomic number of Sn is higher than that of Co. Their magnified HAADF-STEM images at the interface between Li_2SnO_3 and $LiCoO_2$ (corresponding to the squares in Figure 3a,d) are displayed in Figure 3b,e, respectively. Their corresponding FFT patterns indicate that the zone axes of $LiCoO_2$ and Li_2SnO_3 are [010] and [310], respectively, as shown in Figure 3c,f. Panels a and b of Figure 3 clearly show the continuous layered structures of Li_2SnO_3 and $LiCoO_2$ without dislocations. In addition, since the zone axes of $LiCoO_2$ ([010]) and Li_2SnO_3 ([310]) are perpendicular to the [001] direction of $LiCoO_2$ and Li_2SnO_3, this implies that Li_2SnO_3 nanolayers on the $LiCoO_2$ surface were vertically aligned along the [001] direction. Figure 3j shows the line profile of the STEM image intensity across the interface through line 1 along the [001] direction in Figure 3b. The interlayer distances in the dark and the bright regions, respectively, are approximately 4.65 and 4.94 Å. They are almost the same as the interlayer distances of $LiCoO_2$ (4.677 Å) and Li_2SnO_3 (4.937 Å) along the [001] direction. This indicates that the solubility of Sn in $LiCoO_2$ is negligible at 900 °C, which is consistent with the XRD results (Figure 1a). Consequently, this suggests that, since the solubility of Sn in $LiCoO_2$ decreases with increasing temperature, Sn-doped $LiCoO_2$ obtained at 700 °C decomposes gradually with further increasing temperature. Eventually, Li_2SnO_3 was grown outside on the $LiCoO_2$ surface at 900 °C.

For the quenched 5 at. % Sn-added $Li[Ni_xCo_{1-x}]O_2$ ($x = 0$), however, Li_2SnO_3 domains were observed inside a $LiCoO_2$ particle. This is supported by the line profiles of the STEM image intensity through lines 2, 3, and 4, respectively, in each region of dark, interface, and bright areas, as shown in Figure 3e. The interlayer distance is approximately 4.65 Å in the dark region and is 4.94 Å in the bright region. This indicates that the inside domain and the outside area of the quenched sample are Li_2SnO_3 and $LiCoO_2$, respectively. This is opposite to the result for the slowly cooled sample. The different morphologies between the slowly cooled and quenched samples suggest that Li_2SnO_3 was diffused out during a slow cooling process, because the (001) surface of Li_2SnO_3 is more stable than that of $LiCoO_2$. It is also notable that, in contrast to the ordered interface in Figure 3b,j, the disordered grain boundary was observed at the lateral interface through line 3, as shown in Figure 3e,k. This is due to the large lattice mismatch at the

https://dx.doi.org/10.1021/acs.jpclett.0c01829
J. Phys. Chem. Lett. 2020, 11, 7096–7102

lateral interface between the Li_2SnO_3 and $LiCoO_2$ planes. The disordered boundary is also generally less stable than the ordered boundary. Therefore, we suggest that the plane-selective growth of Li_2SnO_3 on the $LiCoO_2$ basal plane occurred to suppress the disordered boundaries.

Five at. % Sn-added $Li[Ni_xCo_{1-x}]O_2$ (x = 0.5) also showed the plane-selective growth of Li_2SnO_3 on the $Li[Ni_{0.5}Co_{0.5}]O_2$ basal plane. Figure 3g shows the cross-sectional HAADF-STEM images of 5 at. % Sn-added $Li[Ni_{0.5}Co_{0.5}]O_2$ obtained at slow cooling rate. Figure 3h shows the atomic resolution Z-contrast HAADF image of the red square area in Figure 3g. The ordered interface between $Li[Ni_{0.5}Co_{0.5}]O_2$ and Li_2SnO_3 was clearly observed. The corresponding FFT pattern supports that Li_2SnO_3 on the $Li[Ni_{0.5}Co_{0.5}]O_2$ layers were vertically aligned (Figure 3h). Figure 3l shows the line profile of the STEM image intensity across the interface through line 5 along the [001] direction in Figure 3h. The interlayer distances in $Li[Ni_{0.5}Co_{0.5}]O_2$ and Li_2SnO_3 regions were approximately 4.75 and 4.94 Å, respectively. They are consistent with the lattice parameters obtained from the XRD Rietveld refinement (Figure 1d).

To demonstrate the role of the basal-plane-selective coating in electrochemical performance, we compared the rate and cycle performances of plane-selective $Li[Ni_xCo_{1-x}]O_2$–Li_2SnO_3 (x = 0) core–shells with those of conventional Li_2SnO_3-coated $LiCoO_2$. (Figure 4). Conventional coating of Li_2SnO_3 on bare $LiCoO_2$ was carried out using a sol–gel synthesis.[32,33] The sol–gel coating of Li_2SnO_3 was not plane-selective, and Li_2SnO_3 islands were randomly coated on all facets of $LiCoO_2$ (Figure S4). The rate performance of $LiCoO_2$ was evaluated at various C rates from 0.1 (16 mA g^{-1}) to 10 C (1.6 A g^{-1}) rates in the voltage range 3.0–4.5 V (vs Li/Li^+). The plane-selective $LiCoO_2$–Li_2SnO_3 core–shell showed remarkably better rate performance than did the conventional sol–gel-derived Li_2SnO_3-coated $LiCoO_2$, as shown in Figure 4a. The corresponding voltage profiles are presented in Figure S5. Li^+ ions are intercalated and deintercalated into $LiCoO_2$ through edge planes along the in-plane direction (normal to the [001] direction). The coating layers of the conventional sol–gel-derived Li_2SnO_3-coated $LiCoO_2$ partially cover the charge-transfer planes, which are edge planes normal to the in-plane direction, as shown in Figure 4b, because the conventional coating was not plane-selective. This coating layer hinders the charge transfer of Li^+ ions, resulting in an increase in charge-transfer resistance. However, the basal-plane-selective $LiCoO_2$–Li_2SnO_3 core–shell did not increase charge-transfer resistance, because the Li_2SnO_3 nanolayers were selectively coated only on the $LiCoO_2$ basal plane, except for the charge-transfer planes (Figure 4c). This was supported by the impedance analysis of $LiCoO_2/LiCoO_2$ symmetric cells. The basal-plane-selective $LiCoO_2$–Li_2SnO_3 core–shell showed a lower charge-transfer resistance (smaller semicircle) than did the conventional Li_2SnO_3-coated $LiCoO_2$ (Figure 4d). The cycle performances of the plane-selective $Li[Ni_xCo_{1-x}]O_2$–Li_2SnO_3 (x = 0 and 0.5) core–shell were also better than the conventional Li_2SnO_3-coated $Li[Ni_xCo_{1-x}]O_2$–Li_2SnO_3 (x = 0 and 0.5) (Figure 4e and Figure S6, respectively). Their corresponding Coulombic efficiencies are presented in Figure S7. This suggests that the plane-selective core–shell shape is also beneficial for suppressing the transition metal dissolution and irreversible electrolyte decomposition at high voltages (>4.3 V vs Li/Li^+). We also examined the electrochemical performance of $LiCoO_2$ with various amounts of Li_2SnO_3 shells from 1 to 5 at. %. Even the small shell amount of 1 at. % Li_2SnO_3 exhibited excellent cycle performance over 100 cycles with a high reversible capacity of 191 mA h g^{-1} (Figure S8). In addition, the plane-selective $LiCoO_2$–Li_2SnO_3 core–shell showed stable capacity retention even at the elevated temperature, 60 °C (Figure S9).

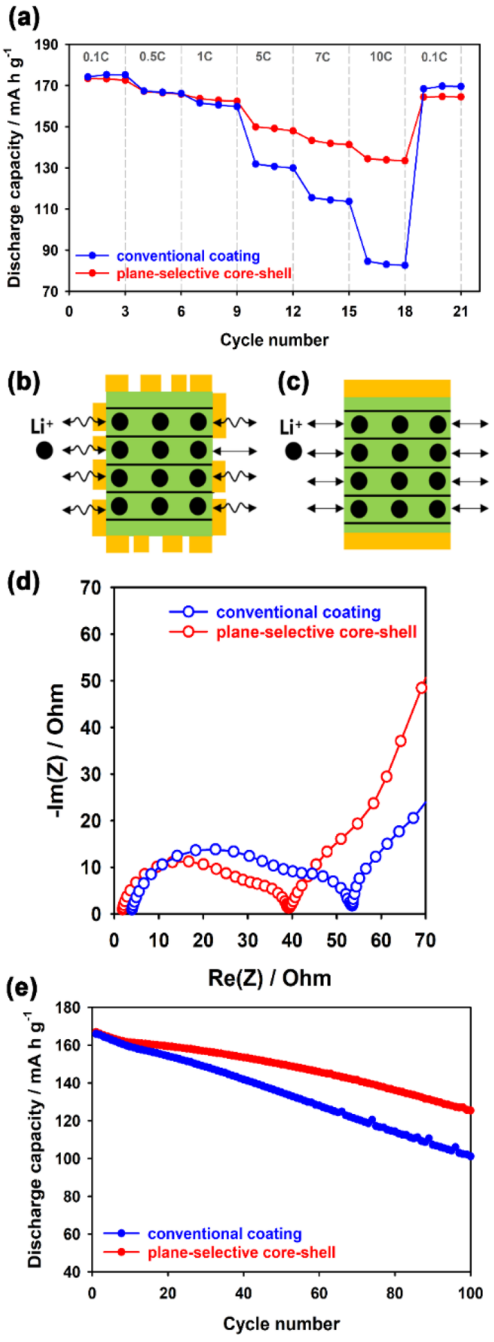

Figure 4. (a) Rate performances of plane-selective $LiCoO_2$–Li_2SnO_3 core–shell and conventional sol–gel-derived Li_2SnO_3-coated $LiCoO_2$. Schematic charge transfer of Li^+ ions for (b) conventional sol–gel-derived Li_2SnO_3-coated $LiCoO_2$ and (c) plane-selective $LiCoO_2$–Li_2SnO_3 core–shell. (d) Nyquist plots of $LiCoO_2/LiCoO_2$ symmetric cells for conventional sol–gel-derived Li_2SnO_3-coated $LiCoO_2$ and plane-selective $LiCoO_2$–Li_2SnO_3 core–shell. (e) Cycle performance of conventional sol–gel-derived Li_2SnO_3-coated $LiCoO_2$ and plane-selective $LiCoO_2$–Li_2SnO_3 core–shell at 1C rate.

https://dx.doi.org/10.1021/acs.jpclett.0c01829
J. Phys. Chem. Lett. 2020, 11, 7096–7102

In summary, we demonstrated the basal-plane-selective coating of Li_2SnO_3 on a $Li[Ni_xCo_{1-x}]O_2(001)$ surface (x = 0 and 0.5) using one-pot synthesis through the solubility variation of Sn in $Li[Ni_xCo_{1-x}]O_2$ with respect to temperature. Our theoretical DFT calculation revealed that the mixture of Li_2SnO_3 and $LiCoO_2$ becomes thermodynamically more stable than Sn-doped $LiCoO_2$ with increasing temperature. This implies that the solubility of Sn in $Li[Ni_xCo_{1-x}]O_2$ decreases with increasing temperature. As a result, we observed that Sn-doped $LiCoO_2$ was segregated into Li_2SnO_3 and $Li[Ni_xCo_{1-x}]O_2$ with increasing heating temperature. Moreover, Li_2SnO_3 nanolayers grew selectively only on the $Li[Ni_xCo_{1-x}]O_2$ basal plane, forming the vertical heterostructure of $Li[Ni_xCo_{1-x}]O_2$–Li_2SnO_3 core–shells. The basal-plane-selective growth of Li_2SnO_3 was attributed to the lattice mismatch at the lateral interfaces between Li_2SnO_3 and $Li[Ni_xCo_{1-x}]O_2$ planes. We also compared the electrochemical performances of the plane-selective $Li[Ni_xCo_{1-x}]O_2$–Li_2SnO_3 core–shells (x = 0 and 0.5) and conventional sol–gel-derived Li_2SnO_3-coated $Li[Ni_xCo_{1-x}]O_2$ at a high voltage range of 3.0–4.5 V (vs Li/Li^+). The plane-selective $Li[Ni_xCo_{1-x}]O_2$–Li_2SnO_3 core–shells showed better rate and cycle performances than did the conventional Li_2SnO_3-coated $Li[Ni_xCo_{1-x}]O_2$. We believe that the interphase engineering of plane-selective surface modifications are promising for cathode materials demanding excellent charge transfer at interphase between electrolytes and active materials.

■ ASSOCIATED CONTENT

Supporting Information

The Supporting Information is available free of charge at https://pubs.acs.org/doi/10.1021/acs.jpclett.0c01829.

Experimental details, detailed DFT calculation, crystal structures, theoretical Helmholtz free energy variations, SEM images, STEM-EDS images, XRD analysis, voltage profiles, Cycle performances, and Coulombic efficiencies (PDF)

■ AUTHOR INFORMATION

Corresponding Authors

Won Bo Lee − *School of Chemical and Biological Engineering, Institute of Chemical Processes, Seoul National University, Seoul 08826, Republic of Korea;* orcid.org/0000-0001-7801-083X; Email: wblee@snu.ac.kr

Kyu Tae Lee − *School of Chemical and Biological Engineering, Institute of Chemical Processes, Seoul National University, Seoul 08826, Republic of Korea;* orcid.org/0000-0003-2769-3372; Email: ktlee@snu.ac.kr

Authors

Hanseul Kim − *School of Chemical and Biological Engineering, Institute of Chemical Processes, Seoul National University, Seoul 08826, Republic of Korea*

Garam Choi − *School of Chemical and Biological Engineering, Institute of Chemical Processes, Seoul National University, Seoul 08826, Republic of Korea*

Seongmin Kim − *School of Chemical and Biological Engineering, Institute of Chemical Processes, Seoul National University, Seoul 08826, Republic of Korea*

Donghoon Lee − *School of Chemical and Biological Engineering, Institute of Chemical Processes, Seoul National University, Seoul 08826, Republic of Korea; Center for Nanoparticle Research, Institute for Basic Science (IBS), Seoul 08826, Republic of Korea*

Sung Wook Doo − *School of Chemical and Biological Engineering, Institute of Chemical Processes, Seoul National University, Seoul 08826, Republic of Korea*

Jungwon Park − *School of Chemical and Biological Engineering, Institute of Chemical Processes, Seoul National University, Seoul 08826, Republic of Korea; Center for Nanoparticle Research, Institute for Basic Science (IBS), Seoul 08826, Republic of Korea;* orcid.org/0000-0003-2927-4331

Complete contact information is available at: https://pubs.acs.org/10.1021/acs.jpclett.0c01829

Author Contributions

#H. Kim, G. Choi, and S. Kim contributed equally to this work.

Notes

The authors declare no competing financial interest.

■ ACKNOWLEDGMENTS

This work was supported in part by the National Research Foundation of Korea (NRF) grant funded by the Korea government (MSIT) (NRF-2019R1A2B5B03070673, NRF-2020M3H4A1A03082968, NRF-2018M3D1A1058633, and NRF-2018R1A5A1024127) and by Technology Development Program to Solve Climate Changes (NRF-2018M1A2A2063345) through NRF funded by Ministry of Science and ICT, and by IBS-R006-D1.

■ REFERENCES

(1) Lee, W.; Muhammad, S.; Sergey, C.; Lee, H.; Yoon, J.; Kang, Y. − M.; Yoon, W.-S. Advances in the Cathode Materials for Lithium Rechargeable Batteries. *Angew. Chem., Int. Ed.* **2020**, *59*, 2578−2605.

(2) Culver, S. P.; Koerver, R.; Zeier, W. G.; Janek, J. On the Functionality of Coatings for Cathode Active Materials in Thiophosphate-Based All-Solid-State Batteries. *Adv. Energy Mater.* **2019**, *9*, 1900626.

(3) Park, K.; Yu, B. − C.; Jung, J. − W.; Li, Y.; Zhou, W.; Gao, H.; Son, S.; Goodenough, J. B. Electrochemical Nature of the Cathode Interface for a Solid-State Lithium-Ion Battery: Interface between $LiCoO_2$ and Garnet $Li_7La_3Zr_2O_{12}$. *Chem. Mater.* **2016**, *28*, 8051−8059.

(4) Li, S.; Li, K.; Zheng, J.; Zhang, Q.; Wei, B.; Lu, X. Structural Distortion-Induced Charge Gradient Distribution of Co Ions in Delithiated $LiCoO_2$ Cathode. *J. Phys. Chem. Lett.* **2019**, *10*, 7537−7546.

(5) Lee, Y.; Lee, T. K.; Kim, S.; Lee, J.; Ahn, Y.; Kim, K.; Ma, H.; Park, G.; Lee, S. − M.; Kwak, S. K.; et al. Fluorine-incorporated Interface Enhances Cycling Stability of Lithium Metal Batteries with Ni-rich NCM Cathodes. *Nano Energy* **2020**, *67*, 104309.

(6) Xie, Y.; Gao, H.; Gim, J.; Ngo, A. T.; Ma, Z. − F.; Chen, Z. Identifying Active Sites for Parasitic Reactions at the Cathode−Electrolyte Interface. *J. Phys. Chem. Lett.* **2019**, *10*, 589−594.

(7) Li, W.; Dolocan, A.; Oh, P.; Celio, H.; Park, S.; Cho, J.; Manthiram, A. Dynamic Behaviour of Interphases and its Implication on High-Energy-Density Cathode Materials in Lithium-ion Batteries. *Nat. Commun.* **2017**, *8*, 14589.

(8) Park, K.; Kaup, K.; Assoud, A.; Zhang, Q.; Wu, X.; Nazar, L. F. High-Voltage Superionic Halide Solid Electrolytes for All-Solid-State Li ion Batteries. *ACS Energy Lett.* **2020**, *5*, 533−539.

(9) Ong, P. − V.; Yang, Z.; Sushko, P. V.; Du, Y. Formation, Structural Variety, and Impact of Antiphase Boundaries on Li Diffusion in $LiCoO_2$ Thin-Film Cathodes. *J. Phys. Chem. Lett.* **2018**, *9*, 5515−5520.

(10) Myung, S.-T.; Noh, H.-J.; Yoon, S.-J.; Lee, E.-J.; Sun, Y.-K. Progress in High-Capacity Core−Shell Cathode Materials for

Rechargeable Lithium Batteries. *J. Phys. Chem. Lett.* **2014**, *5* (4), 671−679.
(11) Park, K.-J.; Hwang, J.-Y.; Ryu, H.-H.; Maglia, F.; Kim, S.-J.; Lamp, P.; Yoon, C. S.; Sun, Y.-K. Degradation Mechanism of Ni-Enriched NCA Cathode for Lithium Batteries: Are Microcracks Really Critical? *ACS Energy Lett.* **2019**, *4* (6), 1394−1400.
(12) You, Y.; Celio, H.; Li, J.; Dolocan, A.; Manthiram, A. Modified High-Nickel Cathodes with Stable Surface Chemistry Against Ambient Air for Lithium-Ion Batteries. *Angew. Chem., Int. Ed.* **2018**, *57* (22), 6480−6485.
(13) Tan, H.; Takeuchi, S.; Bharathi, K. K.; Takeuchi, I.; Bendersky, L. A. Microscopy Study of Structural Evolution in Epitaxial $LiCoO_2$ Positive Electrode Films during Electrochemical Cycling. *ACS Appl. Mater. Interfaces* **2016**, *8*, 6727−6735.
(14) Han, B.; Qian, D.; Risch, M.; Chen, H.; Chi, M.; Meng, Y. S.; Shao-Horn, Y. Role of $LiCoO_2$ Surface Terminations in Oxygen Reduction and Evolution Kinetics. *J. Phys. Chem. Lett.* **2015**, *6*, 1357−1362.
(15) Li, Y.; Chen, X.; Dolocan, A.; Cui, Z.; Xin, S.; Xue, L.; Xu, H.; Park, K.; Goodenough, J. B. Garnet Electrolyte with an Ultralow Interfacial Resistance for Li-Metal Batteries. *J. Am. Chem. Soc.* **2018**, *140* (20), 6448−6455.
(16) Duffiet, M.; Blangero, M.; Cabelguen, P. − E.; Delmas, C.; Carlier, D. Influence of the Initial Li/Co Ratio in $LiCoO_2$ on the High-Voltage Phase-Transitions Mechanisms. *J. Phys. Chem. Lett.* **2018**, *9*, 5334−5338.
(17) Sun, C.; Liao, X.; Xia, F.; Zhao, Y.; Zhang, L.; Mu, S.; Shi, S.; Li, Y.; Peng, H.; Tendeloo, G. V.; et al. High-Voltage Cycling Induced Thermal Vulnerability in $LiCoO_2$ Cathode: Cation Loss and Oxygen Release Driven by Oxygen Vacancy Migration. *ACS Nano* **2020**, *14*, 6181−6190.
(18) Gilbert, J. A.; Shkrob, I. A.; Abraham, D. P. Transition Metal Dissolution, Ion Migration, Electrocatalytic Reduction and Capacity Loss in Lithium-Ion Full Cells. *J. Electrochem. Soc.* **2017**, *164* (2), A389−A399.
(19) Wandt, J.; Freiberg, A.; Thomas, R.; Gorlin, Y.; Siebel, A.; Jung, R.; Gasteiger, H. A.; Tromp, M. Transition Metal Dissolution and Deposition in Li ion Batteries Investigated by Operando X-ray Absorption Spectroscopy. *J. Mater. Chem. A* **2016**, *4* (47), 18300−18305.
(20) Zhou, A.; Liu, Q.; Wang, Y.; Wang, W.; Yao, X.; Hu, W.; Zhang, L.; Yu, X.; Li, J.; Li, H. Al_2O_3 Surface Coating on $LiCoO_2$ Through a Facile and Scalable Wet-Chemical Method Towards High-Energy Cathode Materials Withstanding High Cutoff Voltages. *J. Mater. Chem. A* **2017**, *5* (46), 24361−24370.
(21) Kim, J. W.; Travis, J. J.; Hu, E.; Nam, K.-W.; Kim, S. C.; Kang, C. S.; Woo, J.-H.; Yang, X.-Q.; George, S. M.; Oh, K. H.; et al. Unexpected High Power Performance of Atomic Layer Deposition Coated $Li[Ni_{1/3}Mn_{1/3}Co_{1/3}]O_2$ Cathodes. *J. Power Sources* **2014**, *254*, 190−197.
(22) Hu, L.; Freeland, J. W.; Cabana, J. Surface Chemistry, Passivation, and Electrode Performance in Core−Shell Architectures of $LiCoO_2$ Nanoplates. *ACS Appl. Energy Mater.* **2019**, *2*, 2149−2160.
(23) Yoon, M.; Dong, Y.; Yoo, Y.; Myeong, S.; Hwang, J.; Kim, J.; Choi, S. − H.; Sung, J.; Kang, S. J.; Li, J.; et al. Unveiling Nickel Chemistry in Stabilizing High-Voltage Cobalt-Rich Cathodes for Lithium-Ion Batteries. *Adv. Funct. Mater.* **2020**, *30*, 1907903.
(24) Shi, Y.; Zhang, M.; Qian, D.; Meng, Y. S. Ultrathin Al_2O_3 Coatings for Improved Cycling Performance and Thermal Stability of $LiNi_{0.5}Co_{0.2}Mn_{0.3}O_2$ Cathode Material. *Electrochim. Acta* **2016**, *203*, 154−161.
(25) Xie, J.; Sendek, A. D.; Cubuk, E. D.; Zhang, X.; Lu, Z.; Gong, Y.; Wu, T.; Shi, F.; Liu, W.; Reed, E. J.; et al. Atomic Layer Deposition of Stable $LiAlF_4$ Lithium Ion Conductive Interfacial Layer for Stable Cathode Cycling. *ACS Nano* **2017**, *11* (7), 7019−7027.
(26) Jung, Y. S.; Cavanagh, A. S.; Dillon, A. C.; Groner, M. D.; George, S. M.; Lee, S.-H. Enhanced Stability of $LiCoO_2$ Cathodes in Lithium-Ion Batteries Using Surface Modification by Atomic Layer Deposition. *J. Electrochem. Soc.* **2010**, *157* (1), A75−A81.
(27) Park, J. S.; Mane, A. U.; Elam, J. W.; Croy, J. R. Amorphous Metal Fluoride Passivation Coatings Prepared by Atomic Layer Deposition on $LiCoO_2$ for Li ion Batteries. *Chem. Mater.* **2015**, *27* (6), 1917−1920.
(28) Gu, R.; Ma, Z.; Cheng, T.; Lyu, Y.; Nie, A.; Guo, B. Improved Electrochemical Performances of $LiCoO_2$ at Elevated Voltage and Temperature with an In Situ Formed Spinel Coating Layer. *ACS Appl. Mater. Interfaces* **2018**, *10*, 31271−31279.
(29) Ahn, J.; Kim, J. H.; Cho, B. W.; Chung, K. Y.; Kim, S.; Choi, J. W.; Oh, S. H. Nanoscale Zirconium-Abundant Surface Layers on Lithium- and Manganese-Rich Layered Oxides for High-Rate Lithium-Ion Batteries. *Nano Lett.* **2017**, *17* (12), 7869−7877.
(30) Guo, S.; Li, Q.; Liu, P.; Chen, M.; Zhou, H. Environmentally Stable Interface of Layered Oxide Cathodes for Sodium-Ion Batteries. *Nat. Commun.* **2017**, *8* (1), 135.
(31) Wu, N.; Zhang, Y.; Guo, Y.; Liu, S.; Liu, H.; Wu, H. Flakelike $LiCoO_2$ with Exposed {010} Facets As a Stable Cathode Material for Highly Reversible Lithium Storage. *ACS Appl. Mater. Interfaces* **2016**, *8*, 2723−2731.
(32) Mou, J.; Deng, Y.; Song, Z.; Zheng, Q.; Lam, K. H.; Lin, D. Excellent rate capability and cycling stability in Li^+-conductive Li_2SnO_3-coated $LiNi_{0.5}Mn_{1.5}O_4$ cathode materials for lithium-ion batteries. *Dalton Trans* **2018**, *47* (20), 7020−7028.
(33) Hu, G.; Zhang, M.; Wu, L.; Peng, Z.; Du, K.; Cao, Y. Enhanced Electrochemical Performance of $LiNi_{0.5}Co_{0.2}Mn_{0.3}O_2$ Cathodes Produced via Nanoscale Coating of Li^+-Conductive Li_2SnO_3. *Electrochim. Acta* **2016**, *213*, 547−556.

https://dx.doi.org/10.1021/acs.jpclett.0c01829
J. Phys. Chem. Lett. 2020, 11, 7096−7102